

Near-field mapping of complex-valued wavevectors of in-plane hyperbolic phonon polaritons in α -MoO₃

Cite as: Appl. Phys. Lett. **120**, 131105 (2022); <https://doi.org/10.1063/5.0078210>

Submitted: 11 November 2021 • Accepted: 17 March 2022 • Published Online: 31 March 2022

 Zhu Yuan, Yunji Meng, Weiliang Ma, et al.



View Online



Export Citation



CrossMark

Lock-in Amplifiers up to 600 MHz



Zurich
Instruments



Near-field mapping of complex-valued wavevectors of in-plane hyperbolic phonon polaritons in α -MoO₃

Cite as: Appl. Phys. Lett. **120**, 131105 (2022); doi: [10.1063/5.0078210](https://doi.org/10.1063/5.0078210)

Submitted: 11 November 2021 · Accepted: 17 March 2022 ·

Published Online: 31 March 2022



View Online



Export Citation



CrossMark

Zhu Yuan,¹ Yunji Meng,² Weiliang Ma,¹ Runkun Chen,¹ Tao Wang,^{3,a)} and Peining Li^{1,a)}

AFFILIATIONS

¹Wuhan National Laboratory for Optoelectronics & School of Optical and Electronic Information, Huazhong University of Science and Technology, Wuhan 430074, China

²School of Information Engineering, Huangshan University, Huangshan 245041, China

³Institute of Functional Nano & Soft Materials (FUNSOM), Soochow University, Suzhou, China

Note: This paper is part of the APL Special Collection on Optical Nanoprobe Spectroscopy and Imaging.

^{a)}Authors to whom correspondence should be addressed: wangtao2019@suda.edu.cn and lipn@hust.edu.cn

ABSTRACT

Hyperbolic phonon polaritons (HPhPs) in α -phase molybdenum trioxide (α -MoO₃) have recently attracted significant attention. They propagate anisotropically along the flake of α -MoO₃ and show anomalously concave wavefronts when being excited by a pointlike source. Such anisotropic propagation is governed by the anisotropic wavevectors of HPhPs, which have been studied in different works. However, extracting the complex-valued wavevectors of all HPhP modes directly from the observed anomalous wavefront remains elusive. Here, we theoretically and experimentally demonstrate that the complex-valued HPhP wavevectors can be accurately quantified by fitting the concave wavefront profiles with a modified damped sine-wave function in all allowed directions. To that end, HPhPs are launched by an infrared antenna on a thin flake of α -MoO₃ and are imaged in real space by using scanning near-field optical microscope. From the recorded concave wavefronts of HPhPs, we have experimentally retraced both the real part and the imaginary part of polariton wavevectors along different propagation directions. Our results are of fundamental importance for analyzing the optical properties of HPhPs in α -MoO₃, which can also be generic to other anisotropic optical/polaritonic systems.

Published under an exclusive license by AIP Publishing. <https://doi.org/10.1063/5.0078210>

Phonon polaritons—quasiparticles of photons coupled with optical phonons—in polar van der Waals (vdW) materials recently draw a lot of attention, owing to their remarkable optical properties such as strong electromagnetic-field concentrations,^{1–4} ultra-long polariton lifetimes,^{1,2,5,6} and extreme polariton anisotropy.^{1,6–14} A particularly interesting example is the phonon polaritons in α -phase molybdenum trioxide (α -MoO₃), which can exhibit strongly anisotropic in-plane propagation.^{6,9,15–21} α -MoO₃ is a representative biaxial polar vdW material [with a permittivity tensor (ϵ_x , ϵ_y , and ϵ_z)], which has three so-called Reststrahlen bands (RBs) located in the mid- and far-infrared ranges.^{9,22} These RBs originate from the optical phonon modes along the three crystallographic directions: [001], [100], and [010] (corresponding to x , y , and z axes in this work), respectively.^{6,9,22} The spectral range of each RB is defined by the frequency ranging from the corresponding transverse-optical (TO) phonon frequency to the longitudinal-optical phonon (LO) frequency.

Interestingly, the permittivity of α -MoO₃ exhibits strong anisotropy within those RBs, yielding two distinct types of anisotropic phonon polaritons existing in α -MoO₃. In the uppermost RB with the frequency range of 957–1007 cm^{−1} [where $\text{Re}(\epsilon_x) > 0$, $\text{Re}(\epsilon_y) > 0$, $\text{Re}(\epsilon_z) < 0$, and $\text{Re}(\epsilon_x) \neq \text{Re}(\epsilon_y)$], α -MoO₃ supports phonon polaritons with their in-plane wavevectors describing an elliptically shaped isofrequency contour (IFC) in k -domain.²² On the other hand, in the other two RBs (the frequency range of 545–850 and 821–963 cm^{−1}, respectively), the two in-plane principal permittivities of α -MoO₃ have different signs [$\text{Re}(\epsilon_x) \cdot \text{Re}(\epsilon_y) < 0$ and $\text{Re}(\epsilon_z) > 0$].²² Thus, α -MoO₃ supports in-plane hyperbolic phonon polaritons (HPhPs) with the wavevectors forming a hyperbolic IFC (called hyperbolic dispersion) in k -space. These two types of polaritons, especially the HPhPs, exhibit strong polariton confinement and ultralow polariton losses,^{6,10} showing great application potential for subwavelength imaging,^{23,24} twisted polaritonic

metasurfaces,^{10,12,13,25} polariton-enhanced infrared sensing,^{26,27} nanoscale directional polariton guiding,^{10,28} and many others.

One of the most striking pictures of HPhPs in α -MoO₃ is the anomalously concave wavefronts, arising when the HPhPs are excited by a point-like local source (e.g., hot spots in an optical antenna).^{9,10} These concave wavefronts are formed by interference of polaritons propagating with a direction-dependent wavevector (complex-valued, $k = q + i\gamma$) at a given frequency, reflecting the fingerprint information of HPhPs (e.g., the wavelength and the damping). Typically, by imaging and subsequently executing the Fourier transform (FT) of those wavefronts, one can extract the real part q of the wavevector for each propagation direction and subsequently obtain the polariton wavelength with $\lambda = 2\pi/q$.

In addition to the polariton wavelength, it is also crucial to measure the propagation loss (determined by γ) of HPhPs in all allowed directions. A few experimental works have studied the propagation loss (e.g., the propagation length and lifetime) of HPhPs, but mainly along the crystallographic direction [100] of α -MoO₃.^{6,9,10} As in this direction, the polariton wavevector \mathbf{k} is parallel to the polariton group velocity \mathbf{v}_g , and then one can determine the damping factor γ by fitting the profile of the concave wavefronts along the [100] direction with a modified damped sine-wave function. However, it is still unknown how to extract γ directly from local-source-generated concave wavefronts (landmark features of HPhPs) in all allowed directions, limiting a comprehensive analysis of HPhP properties and a deep understanding of the HPhP physics.

Here, we systematically present how to analyze and determine the propagation loss of the HPhPs launched by the local optical source. By performing both analytical calculations and numerical simulations, we unambiguously demonstrate that the energy decay of the HPhP fields is governed by the imaginary part of the wavevector component ($k_{\parallel} = q_{\parallel} + i\gamma_{\parallel}$) that is along the direction of \mathbf{v}_g . We show that k_{\parallel} can be accurately quantified by fitting the profiles of the concave wavefronts. Thus, the value of the eigen-wavevector \mathbf{k} can be obtained with the relation of $k = k_{\parallel}/\cos(\theta)$, where θ is the angle between \mathbf{k} and \mathbf{v}_g . Furthermore, we execute infrared nanoimaging experiments to record the concave wavefronts of HPhPs launched by an infrared antenna. Supported by our theoretical results, we can experimentally determine the complex-valued polariton wavevectors from the imaged concave wavefronts. The obtained experimental results are in excellent agreement with the theoretical values.

To begin with, we perform numerical simulations of using a point dipole source to excite the HPhPs on a 100 nm-thick layer of α -MoO₃ [at $\omega = 925 \text{ cm}^{-1}$, $\text{Re}(\epsilon_x) > 0$, $\text{Re}(\epsilon_y) < 0$, details are in Methods, [supplementary material](#)]. Figure 1(a) shows the simulated distributions of the near-field magnitude $|E|$, illustrating the highly anisotropic (ray-like) propagation of HPhPs along the layer. Moreover, as shown in Fig. 1(b), the concave wavefronts of dipole-excited HPhPs can be visualized in the simulated near-field distribution of the component E_z (real part). The FT of those concave wavefronts shows the hyperbolic IFC in k space [Fig. 1(c)]. As discussed in previous studies,^{9,10,29} the strong anisotropy of HPhPs yields the existence of an angle of θ between \mathbf{k} and \mathbf{v}_g [sketched in both Figs. 1(b) and 1(c), for the real space and the k domain, respectively], in contrast to isotropic in-plane polaritons with \mathbf{k} being always parallel to \mathbf{v}_g (i.e., $\theta \equiv 0^\circ$). As shown in Fig. 1(c), θ_k and θ_g are the angles of \mathbf{k} and \mathbf{v}_g with respect to y -axis, respectively, and $\theta = \theta_k + \theta_g$. We note that at a

given ω , the value of θ_g varying with θ_k can be determined from the hyperbolic IFC, and then the value of θ is acquired by $\theta_k + \theta_g$ (Fig. S1, [supplementary material](#)). Moreover, the defined k_{\parallel} is a wavevector component in the direction parallel to \mathbf{v}_g with $k_{\parallel} = k \cos(\theta)$.

In the following, we verify that the propagation loss of HPhPs along each direction of \mathbf{v}_g is determined by γ_{\parallel} (the imaginary part of k_{\parallel}). To this end, we fit the line profiles of the concave wavefronts to extract the complex values of the wavevectors. Figure 1(d) plots two of the profiles (green and blue symbols) of the wavefronts along two distinct \mathbf{v}_g directions ($\theta_g = 0^\circ$ and $\theta_g = 32^\circ$). For the direction of $\theta_g = 0^\circ$ (along y -axis, $\theta = 0^\circ$), $k_{\parallel} = k$ as the wavevector \mathbf{k} is parallel to the group velocity \mathbf{v}_g . Thus, it has been experimentally demonstrated that one can simulate the near-field profile of the HPhPs with a modified damped sine wave function:^{6–8}

$$\text{Re}(E) = r^{-0.5} e^{-\gamma_{\parallel} r} \sin(q_{\parallel} r), \quad (1)$$

where r is the distance away from the source. The factor $r^{-0.5}$ accounts for the two-dimensional energy spreading of the polaritons away from the source. On the other hand, we show that for $\theta > 0^\circ$ (e.g., $\theta_g = 32^\circ$, $\theta = 52^\circ$, here \mathbf{k} being no longer parallel to \mathbf{v}_g), Eq. (1) holds for describing the k_{\parallel} component as the energy flux (along \mathbf{v}_g direction) is determined by k_{\parallel} component. To that end, we fit the two line profiles of the concave wavefronts by using Eq. (1). The fitted results are plotted as solid black lines in Fig. 1(d), showing excellent agreement with the simulation results (the symbols). In this way, we can extract the real and imaginary parts of the wavevector: q_{\parallel} and γ_{\parallel} and plot them as a function of the angle θ_k in Figs. 1(e) and 1(f) (green triangles), respectively. Furthermore, $q(\gamma)$ is obtained by $q_{\parallel}(\gamma_{\parallel})/\cos(\theta)$ in the same figures (blue triangles).

To corroborate the wavevectors fitted from the simulations, we analytically calculate the wavevector k of the HPhPs by^{2,30}

$$k = \frac{\rho}{d} \left[\arctan\left(\frac{\epsilon_1 \rho}{\epsilon_z}\right) + \arctan\left(\frac{\epsilon_2 \rho}{\epsilon_z}\right) + \pi l \right], \quad l = 0, 1, 2, \dots, \quad (2)$$

where ϵ_1 and ϵ_2 are the permittivity of superstrate and substrate, respectively. The parameter ρ is given by $\rho = i\sqrt{\epsilon_z/(\epsilon_x \cos^2 \theta_k + \epsilon_y \sin^2 \theta_k)}$ and $d = 100 \text{ nm}$ is the layer thickness of α -MoO₃. The validity of this analytical equation is proved numerically in the [supplementary material](#) Figs. S2 and S3. Using Eq. (2), we show the calculated q and γ as a function of θ_k in Figs. 1(e) and 1(f) (solid black lines), respectively, which quantitatively fit with the fitted results in all directions (see the blue symbols). Such excellent agreement unambiguously verifies that the k values fitted by our method are accurate. It, thus, reveals that the propagation of dipole-launched HPhPs is, indeed, governed by the component k_{\parallel} parallel to the \mathbf{v}_g -direction. This mechanism accounts for the counterintuitive phenomena in concave wavefront that as θ_k increases, the effective wavelength λ_{\parallel} (along the \mathbf{v}_g -direction) becomes larger as well with the rising q , as shown in Figs. 1(d) and 1(e). Also, it shows that not only the magnitude of \mathbf{k} but also the angle θ between \mathbf{k} and \mathbf{v}_g play a vital role in confinement of HPhPs. Moreover, our results corroborate that the geometric spreading factor $r^{-0.5}$ can be used to fit the anisotropic propagation of dipole-launched HPhPs and extract the wavevector component k_{\parallel} along the direction of \mathbf{v}_g .

For an experimental demonstration, we perform antenna-based polariton wavefront imaging using a scattering-type scanning

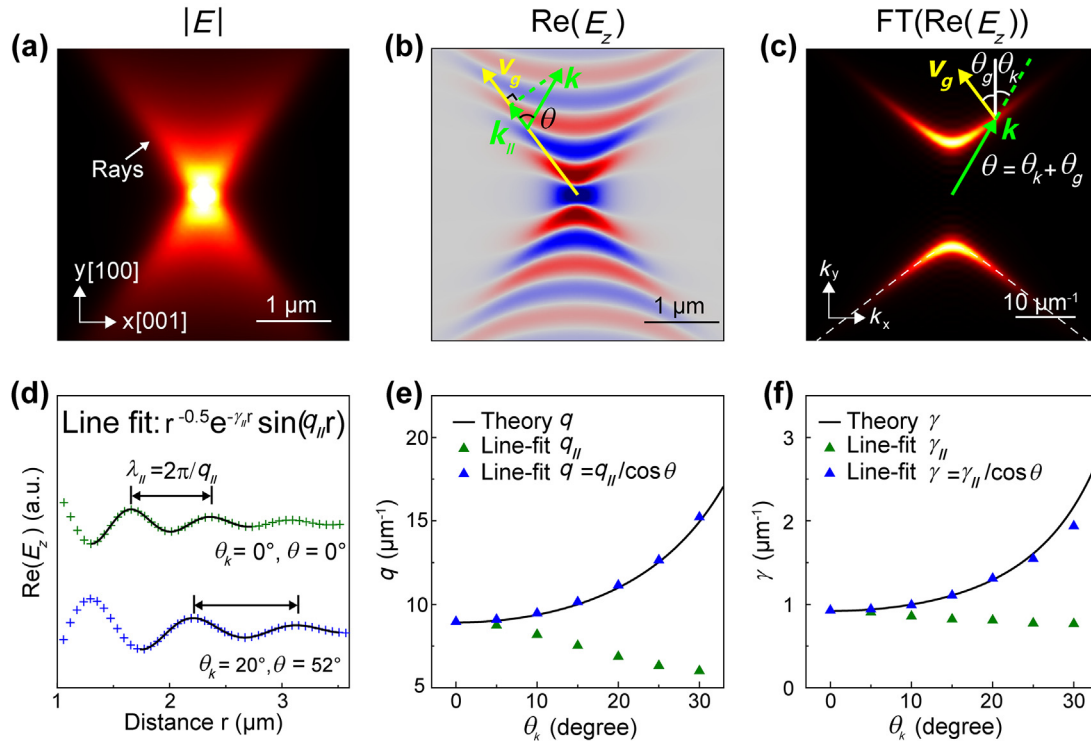


FIG. 1. Numerical simulations for quantifying the complex-valued wavevectors of dipole-excited HPhPs in α -MoO₃. (a) and (b) Simulated near-field magnitude and the real-part of near-fields of HPhPs on a thin layer of α -MoO₃. (c) Fourier transform (FT) of panel (b). White dashed line shows the theoretical IFCs calculated from Eq. (2). (d) Line profiles and the fitting of near-field (b) along the direction of \mathbf{v}_g , as indicated by the yellow arrow in (b). (e) and (f) Real part and imaginary parts of the wavevector of HPhPs as a function of angles θ_k , respectively. Black lines are the theoretical dispersion calculated with Eq. (2). Green symbols are the results of q_{\parallel} and γ_{\parallel} obtained from the fitting [shown in (d)]. Blue symbols are the calculated q and γ by using the values of q_{\parallel} , γ_{\parallel} , and the angle θ .

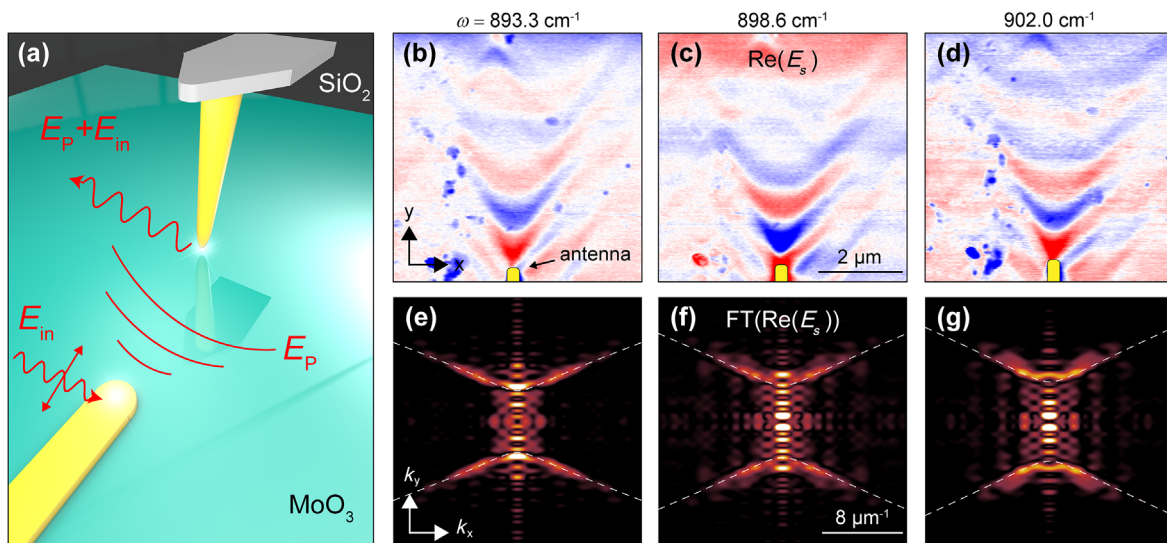


FIG. 2. Near field imaging experiments of antenna-launched HPhPs. (a) Schematic of the experiment. (b)–(d) Near-field images of antenna-launched HPhPs at three different frequencies. (e)–(g) Corresponding FTs of the images (b)–(d), respectively. White dashed lines in (e)–(g) show the calculated theoretical IFCs by using Eq. (2).

near-field optical microscope (s-SNOM).⁹ In the experiment [sketched in Fig. 2(a)], a 3- μm -long Au rod acting as an infrared optical antenna is fabricated on a 220 nm-thick flake of $\alpha\text{-MoO}_3$. A p -polarized mid-infrared laser beam illuminates the antenna. The antenna focuses the illumination and generates hot spots of near fields at the rod extremities for exciting the HPhPs. The launched polaritons propagate along the flake, forming the concave wavefronts, recorded by the tip of s-SNOM. The near-field images [the signal $\text{Re}(E_z)$] recorded at three different frequencies are shown in Figs. 2(b)–2(d) (see also Fig. S4 in the supplementary material), displaying the concave wavefronts of polaritons emitted from the antenna. FT of the imaged wavefronts is shown in Figs. 2(e)–2(g), revealing the hyperbolic IFCs in reciprocal space. These IFCs agree well with the analytical solutions (real part q , dashed white lines) calculated with Eq. (2), revealing deep subwavelength scale confinement ($q > 20k_0$) of HPhPs.

To extract the complex-valued wavevectors from the recorded wavefronts, we fit the experimental line profiles of antenna-launched polaritons using Eq. (1) [see three examples in Fig. 3(a), experimental data: symbols; fitting: solid lines]. Having fitted the parallel components (q_{\parallel} and γ_{\parallel}), we, thus, obtain the intrinsic wavevectors with $k = k_{\parallel}/\cos(\theta)$. Figure 3(b) displays the obtained polariton dispersion $q(\omega)$ for three distinct $\theta_k = 0^\circ$, 20° , and 40° (experimental data: symbols), showing that the value of q (thus the confinement) increases when increasing the frequency. For a fixed frequency, the q value increases with increasing angle θ_k , indicating the larger polariton confinement at larger angles in hyperbolic IFCs.

To better illustrate the angle dependence, we show the value of q as a function of the angle θ_k in Fig. 3(c). It further reveals that the q value increases more quickly at large angles. The experimentally obtained imaginary parts γ of the wavevector are shown in Figs. 3(d)

and 3(e), which exhibit the frequency and angle dependences similar to q . Good agreement between the experimental data [symbols in Figs. 3(b)–3(e)] and analytical solutions [solid lines in Figs. 3(b)–3(e)] finally corroborates the validity of our method for extracting the complex-valued wavevectors of antenna-launched HPhPs. We note that a convincing fitting is challenging to obtain at large θ_k due to a limited signal-noise ratio in the experimental wavefront profiles. We underscore that our method is also applicable to elliptical polaritons in higher band as shown in the supplementary material Fig. S5.

To properly evaluate the angle dependence of the polariton damping, we calculate the ratio $Q = \gamma/q$ as a function of θ_k [Fig. 4(a), experimental data: symbol; analytical solutions: solid lines]. It is clear that the damping ratio r_p almost keeps constant at small angles, while it increases dramatically at large angles (close to the asymptote of the hyperbolic IFC). This observation reveals that the polaritons propagating along small angles exhibit similarly small damping. On the other hand, the polaritons propagating along the asymptote of the hyperbolic IFC exhibit larger damping with their larger wavevectors. To illustrate this observation, we further calculate the material damping ratio $Q_e = |\text{Im}(\epsilon_0)/\text{Re}(\epsilon_0)|$ by using the angle dependence of the $\alpha\text{-MoO}_3$ permittivity ($\epsilon_0 = \epsilon_x \cos^2 \theta_k + \epsilon_y \sin^2 \theta_k$). As shown in Fig. 4(b), the material damping ratio Q_e exhibits a nearly identical angle dependence with the polariton damping Q [see Fig. 4(a)], revealing that the material properties of $\alpha\text{-MoO}_3$ intrinsically determine the propagation properties of HPhPs.

In summary, we propose, theoretically explore, and experimentally demonstrate how to quantify the complex-valued wavevectors from the anisotropic wavefronts of antenna-launched HPhPs propagating along the flake of MoO_3 . We show that the parallel wavevector components k_{\parallel} can be accurately quantified by fitting the profiles of

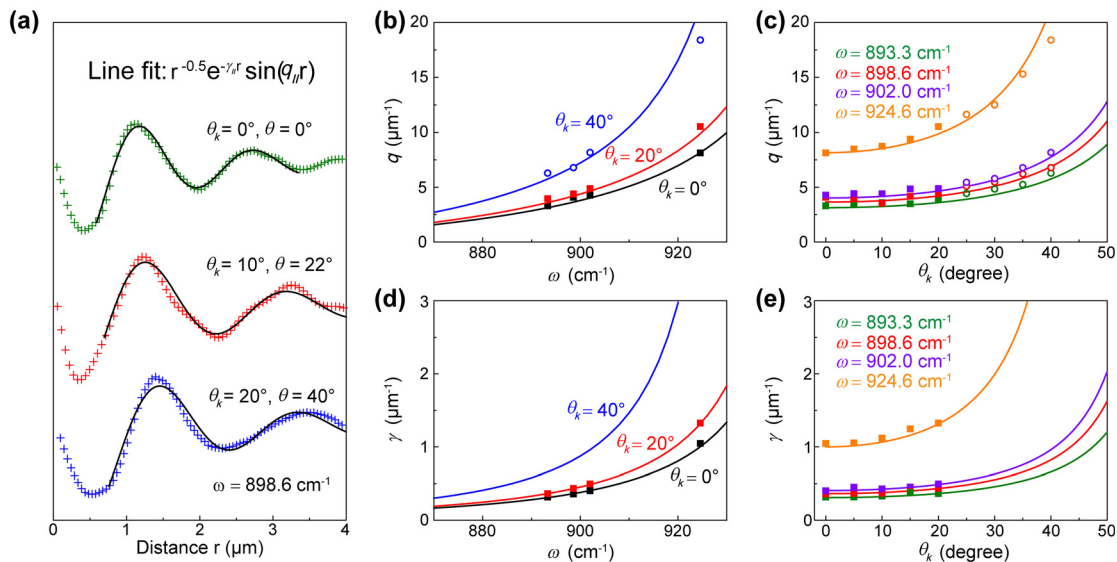


FIG. 3. Experimental quantification of the complex-valued wavevectors of antenna-excited HPhPs. (a) Symbols: line profiles of HPhPs taken from Fig. 2(c). Solid lines: the fitting. (b) Experimental (symbols) and theoretical (solid lines) polariton dispersion at different angles, $\theta_k = 0^\circ$ (black), 20° (red), and 40° (blue). (c) Experimental (symbols) and theoretical (solid lines) angle-dependence of q at different frequencies, $\omega = 893.3 \text{ cm}^{-1}$ (green), 898.6 cm^{-1} (red), 902.0 cm^{-1} (purple), and 924.6 cm^{-1} (orange). (d) Experimental (symbols) and theoretical (solid lines) results of γ at three different angles. (e) Experimental (symbols) and theoretical (solid lines) angle-dependence of γ at different frequencies. The solid squares in (b)–(e) are experimental data obtained from line fit. The open circles in (b) and (c) are experimental data extracted from FT such as the ones shown in Figs. 2(d)–2(f). The theoretical results are calculated using Eq. (2).

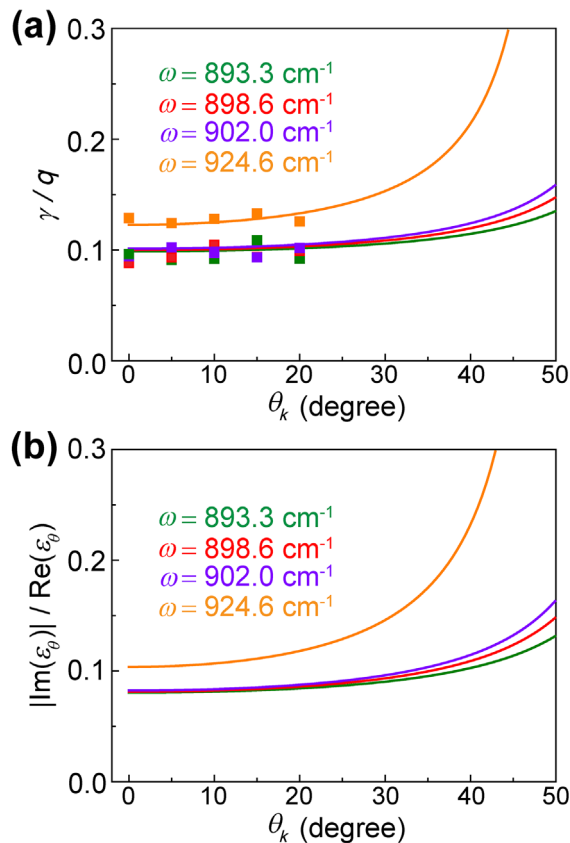


FIG. 4. Determining the angle dependence of polariton damping. (a) Experimental (symbols) and theoretical (solid lines) polariton damping ratio $Q = \gamma/q$ as an action of θ_k at four different frequencies. (b) The ratio $Q_\epsilon = |\text{Im}(\epsilon_\theta)/\text{Re}(\epsilon_\theta)|$ of the angle-dependent permittivity of $\alpha\text{-MoO}_3$ ($\epsilon_\theta = \epsilon_x \cos^2 \theta_k + \epsilon_y \sin^2 \theta_k$) at four different frequencies.

the concave wavefronts along the direction of \mathbf{v}_g with the geometric spreading factor $r^{-0.5}$. Thus, the value of the eigen-wavevector \mathbf{k} can be obtained with the relation of $k = k_{||}/\cos(\theta)$. Supported by our theoretical results, we experimentally determine complex-valued polariton wavevectors of antenna-launched HPhPs from the imaged concave wavefronts. We show that the angle-dependent polariton damping of HPhPs is explained by the intrinsic material losses of $\alpha\text{-MoO}_3$. Our results address a vital question hindering the research of HPhPs and establish a fundamental basis for analyzing the properties of anisotropic polaritonic/optical systems.

See the [supplementary material](#) for methods of the research and more information that supports the results in main text.

P.L. acknowledges the support from the National Natural Science Foundation of China (Grant No. 62075070). T.W. acknowledges the support of the startup funding from Soochow University, the 111 program, and the Collaborative Innovation Center of Suzhou Nano Science and Technology (NANO-CIC).

AUTHOR DECLARATIONS

Conflict of Interest

The authors have no conflicts to disclose.

Author Contributions

Z.Y. and Y.M. contributed equally to this work.

DATA AVAILABILITY

The data that support the findings of this study are available from the corresponding authors upon reasonable request.

REFERENCES

- J. D. Caldwell, A. V. Kretinin, Y. Chen, V. Giannini, M. M. Fogler, Y. Francescato, C. T. Ellis, J. G. Tischler, C. R. Woods, A. J. Giles, M. Hong, K. Watanabe, T. Taniguchi, S. A. Maier, and K. S. Novoselov, *Nat. Commun.* **5**(1), 5311 (2014).
- S. Dai, Z. Fei, Q. Ma, A. Rodin, M. Wagner, A. McLeod, M. Liu, W. Gannett, W. Regan, K. Watanabe, T. Taniguchi, M. Thiemens, G. Dominguez, A. Castro Neto, A. Zettl, F. Keilmann, P. Jarillo-Herrero, M. Fogler, and D. Basov, *Science* **343**(6175), 1125 (2014).
- P. Li, X. Yang, T. W. Maß, J. Hanss, M. Lewin, A.-K. Michel, M. Wuttig, and T. Taubner, *Nat. Mater.* **15**(8), 870 (2016).
- S. Dai, W. Fang, N. Rivera, Y. Stehle, B. Y. Jiang, J. Shen, R. Y. Tay, C. J. Ciccarino, Q. Ma, D. Rodan-Legrain, P. Jarillo-Herrero, E. H. T. Teo, M. M. Fogler, P. Narang, J. Kong, and D. N. Basov, *Adv. Mater.* **31**(37), 1806603 (2019).
- A. J. Giles, S. Dai, I. Vurgaftman, T. Hoffman, S. Liu, L. Lindsay, C. T. Ellis, N. Assefa, I. Chatzakis, T. L. Reinecke, J. G. Tischler, M. M. Fogler, J. H. Edgar, D. N. Basov, and J. D. Caldwell, *Nat. Mater.* **17**(2), 134 (2018).
- W. Ma, P. Alonso-González, S. Li, A. Y. Nikitin, J. Yuan, J. Martín-Sánchez, J. Taboada-Gutiérrez, I. Amenabar, P. Li, S. Vélez, C. Tollan, Z. Dai, Y. Zhang, S. Sriram, K. Kalantar-Zadeh, S. Lee, R. Hillenbrand, and Q. Bao, *Nature* **562**(7728), 557 (2018).
- P. Li, I. Dolado, F. Alfaro-Mozaz, A. Y. Nikitin, F. Casanova, L. Hueso, S. Vélez, and R. Hillenbrand, *Nano Lett.* **17**(1), 228 (2017).
- P. Li, I. Dolado, F. J. Alfaro-Mozaz, F. Casanova, L. E. Hueso, S. Liu, J. H. Edgar, A. Y. Nikitin, S. Vélez, and R. Hillenbrand, *Science* **359**(6378), 892 (2018).
- Z. Zheng, N. Xu, S. L. Oscurato, M. Tamagnone, F. Sun, Y. Jiang, Y. Ke, J. Chen, W. Huang, W. L. Wilson, A. Ambrosio, S. Deng, and H. Chen, *Sci. Adv.* **5**(5), eaav8690 (2019).
- G. Hu, Q. Ou, G. Si, Y. Wu, J. Wu, Z. Dai, A. Krasnok, Y. Mazon, Q. Zhang, Q. Bao, C. Qiu, and A. Alù, *Nature* **582**(7811), 209 (2020).
- S. Dai, M. Tymchenko, Y. Yang, Q. Ma, M. Pita-Vidal, K. Watanabe, T. Taniguchi, P. Jarillo-Herrero, M. M. Fogler, A. Alù, and D. N. Basov, *Adv. Mater.* **30**(16), 1706358 (2018).
- M. Chen, X. Lin, T. H. Dinh, Z. Zheng, J. Shen, Q. Ma, H. Chen, P. Jarillo-Herrero, and S. Dai, *Nat. Mater.* **19**(12), 1307 (2020).
- J. Duan, N. Capote-Robayna, J. Taboada-Gutiérrez, G. Álvarez-Pérez, I. Prieto, J. Martín-Sánchez, A. Y. Nikitin, and P. Alonso-González, *Nano Lett.* **20**(7), 5323 (2020).
- Q. Zhang, Q. Ou, G. Hu, J. Liu, Z. Dai, M. S. Fuhrer, Q. Bao, and C.-W. Qiu, *Nano Lett.* **21**(7), 3112 (2021).
- J. Duan, G. Álvarez-Pérez, K. V. Voronin, I. Prieto, J. Taboada-Gutiérrez, V. S. Volkov, J. Martín-Sánchez, A. Y. Nikitin, and P. Alonso-González, *Sci. Adv.* **7**(14), eabf2690 (2021).
- T. V. de Oliveira, T. Nörenberg, G. Álvarez-Pérez, L. Wehmeier, J. Taboada-Gutiérrez, M. Obst, F. Hempel, E. J. Lee, J. M. Klopff, I. Errea, A. Y. Nikitin, S. C. Kehr, P. Alonso-González, and L. M. Eng, *Adv. Mater.* **33**(2), 2005777 (2021).
- Z. Dai, G. Hu, G. Si, Q. Ou, Q. Zhang, S. Balendhran, F. Rahman, B. Y. Zhang, J. Z. Ou, G. Li, A. Alù, C. Qiu, and Q. Bao, *Nat. Commun.* **11**(1), 6086 (2020).
- Y. Wu, Q. Ou, Y. Yin, Y. Li, W. Ma, W. Yu, G. Liu, X. Cui, X. Bao, J. Duan, G. Álvarez-Pérez, Z. Dai, B. Shabbir, N. Medhekar, X. Li, C. Li, P. Alonso-González, and Q. Bao, *Nat. Commun.* **11**(1), 2646 (2020).

- ¹⁹Y. Wu, Q. Ou, S. Dong, G. Hu, G. Si, Z. Dai, C. W. Qiu, M. S. Fuhrer, S. Mookapati, and Q. Bao, *Adv. Mater.* **33**, 2008070 (2021).
- ²⁰W. Dong, R. Qi, T. Liu, Y. Li, N. Li, Z. Hua, Z. Gao, S. Zhang, K. Liu, J. Guo, and P. Gao, *Adv. Mater.* **32**(46), 2002014 (2020).
- ²¹W. Huang, F. Sun, Z. Zheng, T. G. Folland, X. Chen, H. Liao, N. Xu, J. D. Caldwell, H. Chen, and S. Deng, *Adv. Sci.* **8**, 2004872 (2021).
- ²²G. Álvarez-Pérez, T. G. Folland, I. Errea, J. Taboada-Gutiérrez, J. Duan, J. Martín-Sánchez, A. I. Tresguerres-Mata, J. R. Matson, A. Bylinkin, M. He, W. Ma, Q. Bao, J. I. Martín, J. D. Caldwell, A. Y. Nikitin, and P. Alonso-González, *Adv. Mater.* **32**(29), 1908176 (2020).
- ²³S. Dai, Q. Ma, T. Andersen, A. Mcleod, Z. Fei, M. Liu, M. Wagner, K. Watanabe, T. Taniguchi, M. Thiemens, F. Keilmann, P. Jarillo-Herrero, M. M. Fogler, and D. N. Basov, *Nat. Commun.* **6**(1), 6963 (2015).
- ²⁴P. Li, M. Lewin, A. V. Kretinin, J. D. Caldwell, K. S. Novoselov, T. Taniguchi, K. Watanabe, F. Gaussmann, and T. Taubner, *Nat. Commun.* **6**(1), 7507 (2015).
- ²⁵Z. Zheng, F. Sun, W. Huang, J. Jiang, R. Zhan, Y. Ke, H. Chen, and S. Deng, *Nano Lett.* **20**(7), 5301 (2020).
- ²⁶M. Autore, P. Li, I. Dolado, F. J. Alfaro-Mozaz, R. Esteban, A. Atxabal, F. Casanova, L. E. Hueso, P. Alonso-González, J. Aizpurua, A. Y. Nikitin, S. Vélez, and R. Hillenbrand, *Light* **7**(4), 17172 (2018).
- ²⁷A. Bylinkin, M. Schnell, M. Autore, F. Calavalle, P. Li, J. Taboada-Gutiérrez, S. Liu, J. H. Edgar, F. Casanova, L. E. Hueso, P. Alonso-González, A. Y. Nikitin, and R. Hillenbrand, *Nat. Photonics* **15**(3), 197 (2021).
- ²⁸P. Li, G. Hu, I. Dolado, M. Tymchenko, C.-W. Qiu, F. J. Alfaro-Mozaz, F. Casanova, L. E. Hueso, S. Liu, J. H. Edgar, S. Vélez, A. Alù, and R. Hillenbrand, *Nat. Commun.* **11**(1), 3663 (2020).
- ²⁹E. Yoxall, M. Schnell, A. Y. Nikitin, O. Txoperena, A. Woessner, M. B. Lundeberg, F. Casanova, L. E. Hueso, F. H. Koppens, and R. Hillenbrand, *Nat. Photonics* **9**(10), 674 (2015).
- ³⁰G. Álvarez-Pérez, K. V. Voronin, V. S. Volkov, P. Alonso-González, and A. Y. Nikitin, *Phys. Rev. B* **100**(23), 235408 (2019).